Published as:

Desania R. Govender, Walter W. Focke and William E. Cloete. The burning rate of cast calcium sulfate-aluminium thermites. ACS Appl Mater Interfaces. 2018 Jun 20; 10(24):20679-20687. doi: 10.1021/acsami.8b04205

The Burn Rate of Calcium Sulfate Dihydrate-Aluminum Thermites

Desania R. Govender,[†] Walter W. Focke,[†] Shepherd M. Tichapondwa[†] and William E. Cloete[‡]

[†]Institute of Applied Materials, Department of Chemical Engineering, University of Pretoria, Lynnwood Road, Pretoria, South Africa

E-mail: walter.focke@up.ac.za

[‡] Defence, Peace, Safety & Security, Council for Scientific and Industrial Research, Meiring Naude Road, Pretoria, South Africa

E-mail: BCloete@csir.co.za

KEYWORDS. Thermite, Calcium sulfate dihydrate, Aluminum, Casting, Burn Rate, Combustion

ABSTRACT: The energetics of cast calcium sulfate dihydrate-aluminum thermites were investigated. The casts were prepared from water slurries with a solids content below 65 wt-%. The base case thermite comprised 60 wt-% calcium sulfate dihydrate as the oxidizer with 40 wt-% aluminum as fuel. The heat of hydration of the base case was 83 ± 4 kJ·kg^{-1} (dihydrate basis) and the initial setting time was about 100 min. The compressive strength reached 2.9 ± 0.2 MPa after three days drying in ambient air. The open air burn rate was 12.0 ± 1.6 mm· s^{-1} and a maximum surface temperature of 1370 ± 64 °C was recorded with a pyrometer. Bomb calorimetry indicated an energy output of 8.0 ± 1.1 MJ·kg^{-1}, slightly lower than predicted by the Ekvi thermodynamic simulation. Substitution of 10 wt-% of the oxidant with copper sulfate pentahydrate significantly decreased the initial setting time of the casts to less than 30 min but a secondary aluminum oxidation reaction commenced after 2 h. The density of the castings was varied by either adding hollow sodium borosilicate microspheres or by adding excess water during the casting process. The addition of the hollow glass microspheres caused a decrease in the burning rate. Dehydration of the casts by thermal treatments at either 155 °C or 200 °C led to significant increases in the burning rate.

INTRODUCTION

Pyrotechnic compositions are mixtures of one or more fuels together with at least one oxidizer that burn relatively slowly to produce heat, light, color, gas or smoke effects.[1] Unlike conventional combustion, pyrotechnic reactions do not require the presence of ambient air in order to burn.[2] Pyrotechnics applications are plentiful and include use in airbags, fire extinguishers, and road flares.[3] Thermites are pyrotechnics based on a metal as fuel and are capable of reaching very high reaction temperatures.[2] The non-detonative, self-sustaining and highly exothermic nature of the reaction makes thermites suitable for metal welding or metal-cutting devices. The latter application is the one of present interest

Aluminum is a popular fuel choice because it is inexpensive and readily available. Micron-sized aluminum powder is available in a variety of particle shapes. Flakes have a larger surface area and are more sensitive to ignition. However, batch to batch reproducibility is more consistent with spherical atomized forms.[1] Nanothermites are made up of particles smaller than 100 nm in size. They tend to deflagrate with flame velocities exceeding 1 km·s^{-1}, but they do not detonate.[4] Micron-sized thermites burn much more slowly as the reaction is diffusion-controlled unlike the faster kinetics-controlled reactions in the nano-environment.[4]

Loose micron-sized thermite powders are prone to erratic combustion behavior. Consolidation into monolithic solids with uniform properties improves the consistency of the burning process. Metal sulfates have been employed as oxidizers for both micron- and nano-sized aluminum thermites and it was found that the presence of waters of hydration even increased the heat of reaction.[5] Hydrated salts, e.g. $MgSO_4 \cdot 7H_2O$, provide "solidified" water for reaction with a metal fuel.[6] Ignition of such compositions produces hydrogen gas in addition to the metal oxide. Fortunately the reaction between aluminum and water, while exothermic, proceeds very slowly when the fuel is micron-sized.[7] Freshly prepared aqueous slurries, containing calcium sulfate hemihydrate (i.e. Plaster of Paris), are fluid and can be poured into suitable molds. The slightly exothermic hydration reaction, shown in Scheme I, is responsible for the setting of the cast. Part of the liquid water initially present is incorporated into the solid phase by the hydration reaction itself. The slurry solidifies due to a setting process. The hemihydrate first forms a supersaturated solution in the water that is present from which, subsequently, a compact mass of interlaced needle-shaped calcium sulfate dihydrate crystals is deposited.[8] On drying the excess water evaporates, and a fairly porous solid structure remains. The ultimate aim is to use such gypsum-based slurries as reactive binders for highly energetic thermite systems. The envisioned metal cutting application calls for the rapid setting of such casts. This study is a first step towards this ultimate goal. It reports on the energetics and the burn rate of the calcium sulfate/aluminum system, its mechanical properties and the rate of burning of casts of varying density, in addition to a way to accelerate the setting rate of the Plaster of Paris slurry.

$$CaSO_4 \cdot 0.5H_2O + 1.5\ H_2O \rightarrow CaSO_4 \cdot 2H_2O$$

Scheme I: Plaster of Paris hydration reaction

EXPERIMENTAL SECTION

Materials. Q-Cel® 6019 hollow glass microspheres were purchased from AMT composites, a local distributor of Potters Europe. According to the manufacturers' data sheet, the average particle size is 75 μm and the density is 0.14 g·cm^{-3}. Atomized aluminum powder and anhydrous calcium sulfate were procured from Grinman Pty (Ltd) and Alfa Aesar respectively. Calcium sulfate hemihydrate, sulfur and copper sulfate pentahydrate powders were supplied by SigmaAldrich. X-ray fluorescence (XRF) analysis showed that all the raw materials, except the calcium sulfate hemihydrate, were of high purity, i.e. > 99 wt-%. The calcium sulfate hemihydrate purity exceeded 97 wt-% with MgO as the most significant contaminant at 1.9 wt-%. Scanning electron microscopy (SEM) images of the fuel and oxidizer precursor powders are shown in Figure 1. Table 1 summarizes the physical characteristics of the raw materials.

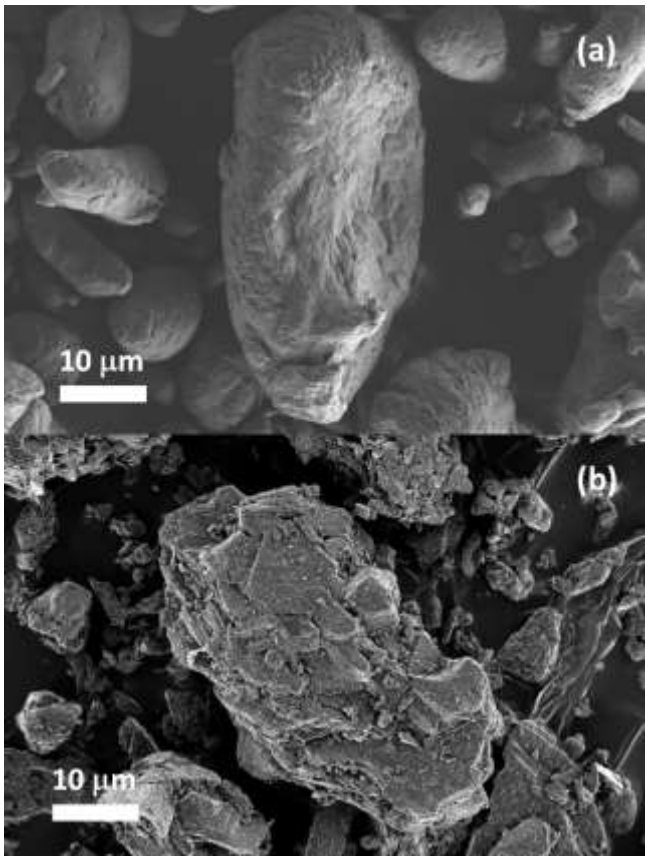

Figure 1. SEM images of the raw material powders: (a) Aluminum powder, and (b) $CaSO_4 \cdot 0.5H_2O$

Modelling. Thermodynamic simulations were performed to determine the effect of fuel to oxidizer ratio on the adiabatic reaction temperature and the nature of the reaction products. Ekvi software[9] was used to compute equilibrium compositions upon the assignment of reaction criteria, which included specifying the reactant ratios, pressure (or volume), temperature and possible products. Initial simulations considered only aluminum as fuel with calcium sulfate (anhydrite, hemihydrate and dihydrate forms) as oxidizer. Additional simulations were performed with the $CaSO_4$ in different hydration states, or with inclusion of either sulfur or copper sulfate pentahydrate. Simulations were also performed in the presence of helium gas pressurized to 3.0 MPa. This was done in order to compare the Ekvi simulation results with bomb calorimeter measurements.

Table 1. Characteristics of raw material powders

Material	D_{50} (μm)	BET[a] ($m^2 \cdot g^{-1}$)	Density ($g \cdot cm^{-3}$)
Al	**13 ± 0**	**0.17**	**2.70**
$CaSO_4 \cdot 0.5H_2O$	**4.5 ± 2.4**	**2.5**	**2.32[b]**
$CaSO_4$	**30 ± 5**	**2.1**	**2.96**
Sulfur	**29 ± 0**	**0.18**	**2.07**
$CuSO_4 \cdot 5H_2O$	**n. a.**	**n. a.**	**2.28**
Microspheres[c]	**57 ± 5**	**n. a.**	**0.14**

[a]BET specific surface area; [b]Dihydrate form; [c]Q-Cel® 6019 hollow microspheres: $SiO_2/Na_2O/B$

Table 2. Cast thermite compositions[*] (wt-%)

Component	Base1	Blend2	S4	CSP5
Aluminum	**40**	**40**	**30**	**40**
Dihydrate[#]	**60**	**30**	**50**	**50**
$CaSO_4$	**-**	**30**	**-**	**-**
Sulfur (S)	**-**	**-**	**20**	**-**
$CuSO_4 \cdot 5H_2O$	**-**	**-**	**-**	**10**

[*]Full hydration of hemihydrate to $CaSO_4 \cdot 2H_2O$ assumed.

Compositions. The base composition, chosen based on the Ekvi simulations, together with three modifications, shown in Table 2, were selected for experimental investigation. The hydration reaction was expected to convert all of the hemihydrate into the dihydrate form. Blend2 was considered in order to study the effect of a partially hydrated oxidant form. It was prepared by substituting part of the hemihydrate with anhydrite which does not react with water. Part of the aluminum fuel was substituted with sulfur in composition S4 while part of the oxidant was substituted with copper sulfate in composition CSP5.

Casting method. It was assumed that the hydration reaction of Scheme I for $CaSO_4 \cdot 2H_2O$ will proceed to completion during the casting of the slurries. This was taken into account when determining the quantities of the individual reagent powders to be used. They were chosen such that the final compositions corresponded to those listed in Table 2. The final casting mass, after full hydration and loss of excess water, was 5.0 g. The $CuSO_4 \cdot 5H_2O$ was ground in a 750 W Pyramid spice grinder for 4 min to obtain a fine powder. The powders were first weighed separately and then combined and brushed through a 125 μm sieve. Excess water was necessary for effective mixing into a homogeneous slurry before setting commenced and also for obtaining a smooth surface finish after setting. Mole ratios of $CaSO_4 \cdot 0.5H_2O$ to H_2O ranging from 1:6 to 1:10 were found to be suitable for casting. In the end a 1:10 mole ratio, corresponding to a slurry solids content of about 65 wt-%, was used. Once

water was added, the compositions were subjected to vigorous stirring. Casts were made in half-cylinder molds and allowed to set and dry at ambient conditions over a period of three days before being weighed and used in testing. Casts with lower density were prepared by adding hollow glass microspheres. In addition, some casts were dehydrated for 2 h at either 155 °C or 200 °C in attempts to convert the calcium dihydrate present to the hemihydrate.

Characterization. The reagent powders were carbon coated with an Emitech K950X coater. Images were taken on a Zeiss Ultra Plus 55 scanning electron microscope (SEM) at a voltage setting of 1 kV. Thin sliver-shaped fragments obtained by fracturing cast samples were deposited on adhesive carbon tape and viewed using a JEOL JSM-IT300LV scanning electron microscope at an accelerating voltage of 2 kV. Phase identification was carried out by XRD analysis on a Rigaku Ultima IV powder diffractometer using Cu-Kα radiation (λ = 0.15406 nm). The PDSL2 software was used for data manipulation.

Particle size distributions were determined with a Malvern Mastersizer 3000, with water as the dispersant. BET specific surface areas were measured on a Micromeritics Tristar II instrument using nitrogen. Samples were degassed for 5 h at 40 °C before measurements were taken.

True density, i.e. the mass of a substance divided by its volume, excluding open and closed pores, was determined with a Micromeritics Accupyc II 1340 pycnometer. Bulk density, i.e. the mass of the material divided by the volume occupied that includes interstitial space, was determined with a Geopyc 1635 envelop density analyzer.

The kinetics of the calcium sulfate hydration reactions were investigated using isothermal heat flow calorimetry[10, 11] at a temperature of 25 °C. The heat flow rate was measured as a function of time and the heat of hydration was determined with a TA Instruments TAM air flow calorimeter. Thermite powder samples (4.00 g) were mixed with 2.00 g of water and the heat flow tracked for 14 h. Duplicate runs were performed for each composition.

Additional cylindrical casts, with a diameter of 15 mm and height of 20 mm, were prepared for mechanical property testing. The compressive strength of these casts were determined using a 5 kN LRX Plus tensile tester. The samples were crushed at a rate of 0.5 mm·min^{-1}. The reported strengths represent averages over at least four measurements.

The energy outputs of the thermites were determined with a Parr 6200 bomb calorimeter and a Parr 6510 water handling system. The bomb vessel was pressurized to 3.0 MPa with helium. About 0.595 g of ground thermite composition was initiated with 0.115 g Starter 1 (containing red lead and silicon) and 0.215 g Starter 2 (containing barium nitrate) in addition to the fuse wire of the bomb calorimeter. The energy contributions of the starters and nichrome wire initiator were taken into account to obtain an overall gross heat release. Three repeats were conducted per composition.

Differential thermal analysis (DTA) was performed on a Shimadzu DTA 50 Differential Thermal Analyzer. Approximately 20 mg powder was placed in alumina crucibles. The reference pan was filled with 20 mg alumina (Al_2O_3) as reference standard. The heating rate was 50 °C·min^{-1} and the temperature was scanned from ambient to 1200 °C with argon flowing at a rate of 20 mL·min^{-1}. At least three repeats were conducted per sample.

Open air burns. Open air burn rate measurements were conducted in a fume hood. Alumina tiles, measuring 100 × 150 mm, were stacked in such a way that a small cage was formed with one side left open. This allowed placement of the cast and facilitated the tracking of the burn event. The latter was done using video recordings with a Dias Infrared Systems Pyroview 380Lc/50Hz/30°×23° infrared (IR) camera and a Raytek RAYMM1MHVF1L pyrometer. The cast was ignited with a sparkler composed mainly of barium nitrate. Burn rates were estimated from the IR camera recordings by dividing the cast length by the burning time period. This was taken to be the time interval from the point where the sample ignited to when the flame stopped propagating forward.

Confined burns. Phenolic tubes with an inner diameter of 15 mm and a depth of 28 mm were oven-dried at 30 °C for several days before use. Thermites samples (ca. 5.3 g) were cast directly into the phenolic tubes. After the compositions set, the tubes were capped with a screw-on graphite nozzle with an outlet diameter of 6.0 mm. The nozzle-capped tubes were then placed in a stainless steel housing and screwed into place with a fastener. A starter composition composed of 41 wt-% copper oxide (CuO), 33 wt-% molybdenum trioxide (MoO_3) and 25 wt-% magnalium (Mg/Al alloy) was used. About 0.5 g starter was poured into the opening of the nozzle. A Vulcan electric fuse head was carefully placed in the opening so that it came into contact with the starter composition. Adhesive aluminum tape was fixed over the nozzle opening to keep the fuse head in place. The test jig was fastened to a metal support structure with cable ties. The prepared sample was then screwed onto the jig in a vertical position with the nozzle facing up. An 80 mm diameter aluminum block was weighed and labelled. It was then clamped onto the jig with the flat surface facing down onto the nozzle opening. The gap between the nozzle and the aluminum block was set at 5.0 mm. The burn rate was estimated from the height of the thermite in the tubes and the burn time extracted from video recordings.

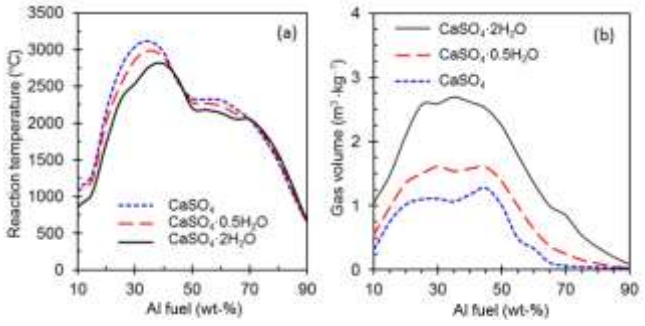

Figure 2. Calcium sulfate-aluminum thermite predictions obtained by Ekvi simulations for a pressure of 0.1 MPa. (a) Adiabatic reaction temperatures; (b) Total gas volume generated

RESULTS AND DISCUSSION

Ekvi simulation results are presented in Figure 2 which shows the effect of fuel content on the adiabatic reaction tem-

perature and the volume of gas evolved. The aluminum-anhydrous calcium sulfate ($Al/CaSO_4$) system reached a maximum reaction temperature of 3100 °C at 33 wt-% Al. The aluminum-calcium sulfate dihydrate ($Al/CaSO_4{\cdot}2H_2O$) system reached a peak reaction temperature of about 2800 °C at 40 wt-% Al. This composition was chosen for experimental verification as it also produced the highest gas volume, i.e. 2.6 $m^3{\cdot}kg^{-1}$ thermite (Figure 2(b)). Moderate gas generation can be a desirable attribute in thermite-based metal cutting applications.

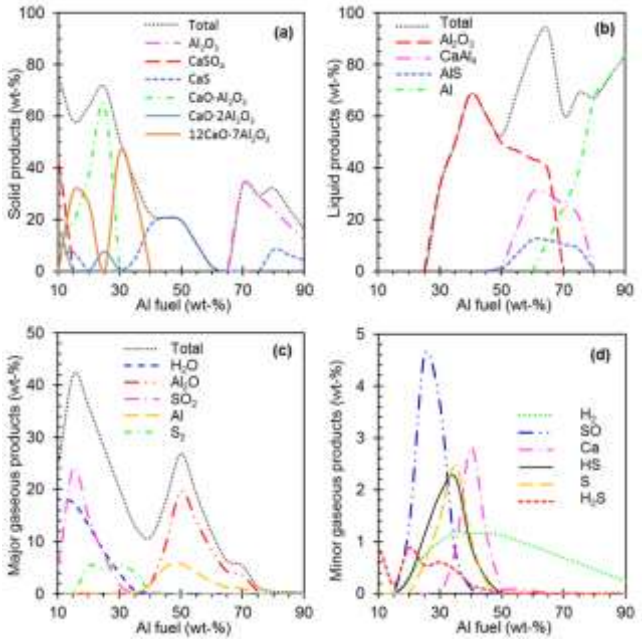

Figure 3. Ekvi -predicted product spectra at a pressure of 0.1 MPa under adiabatic reaction conditions for the $CaSO_4{\cdot}2H_2O$-Al system: (a) Solid; (b) liquid; (c) major gaseous, and (d) minor gaseous products

Ekvi predicted product spectra. Figure 3 summarizes the main reaction products for the $Al/CaSO_4{\cdot}2H_2O$ system formed at a pressure of 0.1 MPa and at the adiabatic reaction temperature. According to Figure 3(a) the most abundant solid phase compounds, present at the lowest fuel loadings, are residual unreacted calcium sulfate together with various calcium aluminates. Between 40 and 65 wt-% Al fuel, calcium sulfide is the only solid product. Above 60 wt-% Al, alumina becomes an important solid product. Figure 3(b) indicates that there is no liquid phase below 25 wt-% Al. Liquid alumina is present between 25 and 70 wt-% Al fuel and it reaches a peak content at 40 wt-% Al. Aluminum sulfide and the intermetallic $CaAl_4$ are important components of the liquid phase in the fuel loading range 50 to 80 wt-%. Both reach their maximum extent at about 60 wt-% Al fuel. Above 60 wt-% unreacted aluminum becomes an important liquid constituent. According to Figure 3(c), at very low fuel loadings, the dominant gaseous products are water and sulfur dioxide with the latter reaching a maximum concentration at about 15 wt-% aluminum. However, at approximately 40 wt-% Al, their concentrations are very low and the dominant gas component, on a mass basis, is calcium vapor although Al and Al_2O vapors are also present. However, on a mole basis, hydrogen is by far the most common gaseous product when the fuel exceeds 15 wt-% Al. Al and Al_2O vapors reach their maximum extents at ca. 50 wt-% Al as fuel. Interestingly, the amount of gas formed on a mass basis reaches peak values at ca. 15 and 50 wt-% while a local minimum is observed at 40 wt-% Al. However, the latter minimum is actually associated with a maximum in the volume of gas formed. Therefore, the main reasons for the maximum in the volume of gas, at that specific fuel content, are the high reaction temperature and the generation of low molar mass H_2 gas.

Principal chemical reactions. The dihydrate form of the calcium sulfate is the main oxidant and it dehydrates according to the reaction shown in Scheme II. The completely anhydrous β-anhydrite form is obtained on heating above 250 °C.

$$CaSO_4{\cdot}2H_2O_{(s)} \rightarrow CaSO_{4(s)} + 2\ H_2O_{(g)}$$

Scheme II. Dehydration reaction of gypsum dihydrate to form anhydrite

$$14\ Al_{(s)} + 12\ CaSO_4{\cdot}2H_2O_{(s)} \rightarrow 12CaO{\cdot}7Al_2O_{3(s)} + 9\ SO_{2(g)} + 3\ H_2S_{(g)} + 21\ H_2O_{(g)}$$

$$4\ Al_{(s)} + 3\ CaSO_4{\cdot}2H_2O_{(s)} \rightarrow CaS_{(s)} + 2\ CaO{\cdot}Al_2O_{3(s)} + 2\ SO_{2(g)} + 6\ H_2O_{(g)}$$

Scheme III. Two reactions controlling the product spectrum at 15.5 wt-% and 17.3 wt-% aluminum fuel respectively

Particular chemical reactions effectively determine the equilibrium product spectra at specific aluminum fuel levels. These reactions can be inferred from the results reported in Figure 3 and they are presented in Scheme III to Scheme VII. However, the situation is more complex and Scheme VIII lists additional reactions responsible for the appearance of specific reaction products in the gas phase.

Scheme III shows two reactions that determine the major reactions products observed at aluminum fuel loadings below 25 wt-% aluminum. Based on the results of the Ekvi simulations, the calcium sulfate reagent is fully converted into other products above 15.5 wt-% Al in the feed. The main condensed phase products are dodecacalcium hepta-aluminate (known as the mineral mayenite) and monocalcium aluminate. The gaseous reaction products include steam and sulfur-based compounds.

$$6\ Al_{(s)} + 3\ CaSO_4{\cdot}2H_2O_{(s)} \rightarrow 3CaO{\cdot}Al_2O_{3(s)} + SO_{(g)} + 0.5\ S_{2(g)} + H_2S_{(g)} + 5\ H_2O_{(g)}$$

Scheme IV. Balanced reaction for an aluminum fuel loadings of 23.9 wt-%

Scheme IV shows the dominant reaction occurring at aluminum fuel loadings near 23.9 wt-%. The main condensed phase product is monocalcium aluminate with sulfur monoxide, hydrogen sulfide and water as the gaseous products.

Scheme V shows the reaction responsible for the formation of gaseous hydrogen and calcium metal. The major condensed products include solid calcium sulfide and molten aluminum oxide (CaS and Al_2O_3) while hydrogen and calcium metal gas

are present in the vapor. Scheme VI shows the reaction dominating at an Al fuel loading near 43.9 wt-%. The major condensed products in this case are solid calcium sulfide and molten aluminum oxide (CaS and Al_2O_3) while hydrogen and Al_2O are present in the gas phase.

$$8\ Al_{(s)} + 2\ CaSO_4{\cdot}2H_2O_{(s)} \rightarrow CaS_{(s)} + 4\ Al_2O_{3(l)} + Ca_{(g)} + 4\ H_{2(g)}$$

Scheme V. Balanced reaction for an aluminum fuel loading of 38.5 wt-%.

$$20\ Al_{(s)} + 4\ CaSO_4{\cdot}2H_2O_{(s)} \rightarrow 4\ CaS_{(s)} + 7\ Al_2O_{3(l)} + 3Al_2O_{(l)} + 8\ H_{2(g)}$$

Scheme VI. Balanced reaction for an aluminum fuel loading of 43.9 wt-%.

$$48\ Al_{(s)} + 4\ CaSO_4{\cdot}2H_2O_{(s)} \rightarrow 5\ Al_2O_{3(l)} + 4\ CaAl_{4(l)} + 9\ Al_2O_{(g)} + 4\ AlS_{(g)} + 8\ H_{2(g)}$$

Scheme VII. Balanced reaction for an aluminum fuel loading of 65.3 wt-%.

Scheme VII shows the reaction that yields, as major condensed products, molten aluminum oxide, aluminum sulfide (AlS), and the intermetallic compound calcium aluminide. Hydrogen and Al_2O are present in the gas phase.

The secondary reactions between sulfur dioxide and hydrogen sulfide and between aluminum and aluminum oxide as well as several disproportionation reactions shown in Scheme IV, complicate the composition of the gas phase over much of the aluminum fuel range. On a mole basis, hydrogen is the dominant gas species over most of the aluminum fuel range.

$$SO_{2(g)} + H_2S_{(g)} \leftrightarrow H_{2(g)} + 2\ SO_{(g)}$$
$$4\ SO_{(g)} \leftrightarrow S_{2(g)} + 2\ SO_{2(g)}$$
$$2\ SO_{(g)} \leftrightarrow S_{(g)} + SO_{2(g)}$$
$$2\ H_2S_{(g)} \leftrightarrow H_{2(g)} + 2HS_{(g)}$$
$$H_2S_{(g)} \leftrightarrow H_{2(g)} + S_{(g)}$$
$$2\ H_2S_{(g)} \leftrightarrow 2\ H_{2(g)} + S_{2(g)}$$
$$3\ Al_2O_{(g)} \leftrightarrow 4\ Al_{(l)} + Al_2O_{3(l)}$$

Scheme VIII. Secondary reactions occurring in the gas phase.

The last reaction listed in Scheme VIII describes a disproportion reaction that happens at high Al fuel loadings. However, it also occurs as the reverse reaction with excess aluminum reacting with alumina to form gaseous Al_2O at low Al fuel loadings, i.e. just above 38.5 wt-%. Furthermore, in the presence of excess aluminum the calcium sulfide is reduced to the intermetallic compound as illustrated in Scheme IX. This conversion happens above about 50 wt-% aluminum fuel.

$$5\ Al_{(s)} + CaS_{(s)} \leftrightarrow CaAl_{4(l)} + AlS_{(l)}$$

Scheme IX. Reduction of calcium sulfide by aluminum

X-ray diffraction phase composition. XRD phase analysis of the residues collected after the burn tests is shown in Table 3. For all compositions, the main condensed products collected from burn tests were aluminum oxide (Al_2O_3), monocalcium dialuminate ($CaO{\cdot}2Al_2O_3$) and aluminum (Al). For Base1, the predominant product was 47 wt-% $CaO{\cdot}2Al_2O_3$ while for Blend2 it was 43 wt-% monocalcium hexa-aluminate ($CaO{\cdot}6Al_2O_3$). In contrast, Al_2O_3 was the most prominent burn product for S4 and CSP5 at 45 wt-% and 53 wt-% respectively.

Table 3. XRD phase analysis on burn residues collected from open air burn tests in wt-%

Burn product	Base1	Blend2	S4	CSP5
Al_2O_3	11	11	45	53
$CaO{\cdot}6Al_2O_3$	24	43	5	13
$CaO{\cdot}2Al_2O_3$	47	22	20	25
CaS	15	22	29	9
Al	2	3	0	0
Total	100	100	100	100
Measured Al/Ca*	2.10	1.98	1.65	4.27
Expected Al/Ca*	2.86	2.53	2.58	3.44

*Mass ratios estimated from XRD data

In comparison, the major condensed products expected from the EKVI simulations for all compositions were $Al_2O_{3(l)}$ and $CaS_{(s)}$. For Base1, it was 69 wt-% Al_2O_3 and 18 wt-% CaS while for Blend2 the major products were 65 wt-% Al_2O_3 and 20 wt-% CaS. Similarly, the major products predicted for S4 were 55 wt-% Al_2O_3 and 20 wt-% CaS while for CSP5 it was 65 wt-% Al_2O_3 and 15 wt-% CaS. These discrepancies do not necessarily indicate that the Ekvi simulations were invalid as they relate to the expected compositions at the corresponding adiabatic reaction temperatures whereas the XRD phase compositions were obtained after the residues had cooled down to ambient. It is possible that further reactions may have occurred during the cooling down process. In addition, the calculated mass ratios of Al/Ca for each composition, given in Table 3 did not match theoretical expectation. The discrepancy could be due to the fact that some amorphous material was also present while the XRD estimates only relate to the crystalline phases present.

Table 4. Heats of hydration and the dry densities of casts

Component	Base1	Blend2	S4	CSP5
Heats of hydration ($kJ{\cdot}kg^{-1}$ dihydrate content)				
	83 ± 4	89 ± 1	81 ± 3	933 ± 8
Dry densities[#] ($g{\cdot}cm^{-3}$)				
ρ calculated	2.46	2.64	2.36	2.45
ρ measured	2.48	2.62	2.34	2.43
ρ_B measured	1.04	1.11	1.06	1.14
ρ_B std. dev.	0.05	0.02	0.02	0.04
Porosity (-)	0.58	0.58	0.55	0.53

[#] ρ and ρ_B are the true and bulk densities respectively.

Heats of hydration. Figure 4 shows the heat release data generated by the isothermal heat flow calorimeter. The results are based on the total slurry mass while the values, reported in Table 4, were normalized with respect to the gypsum content. Figure 4(a) shows that the peak heat flow for Base1, Blend2 and S4 compositions was reached within 1 h of water addition. The peak heat flow for Base1 was 23 ± 3 $W \cdot kg^{-1}$ after 47 ± 8 min. Similarly, the peak heat flow for Blend2 was 10.4 ± 0.9 $W \cdot kg^{-1}$ at 45 ± 2 min and S4 was 15.7 ± 1.4 $W \cdot kg^{-1}$ after 62 ± 12 min. In contrast, the heat release profile for composition CSP5 differed significantly from those obtained for the other compositions. It featured two main heat flow peaks. The first occurring at 11 ± 2 min with a peak value of 42.3 ± 1.5 $W \cdot kg^{-1}$ and the second occurring at 3.18 ± 0.04 h at 77 ± 4 $W \cdot kg^{-1}$.

These observations are in accord with those made during casting which revealed that CSP5 samples solidified significantly faster than the other compositions. The second heat flow peak is attributed to the reaction of the copper sulfate present with the aluminum powder in the composition. Figure 5 shows XRD diffractograms recorded for a sample of the pulverized cast after setting and drying. It shows reflections attributable to copper and aluminum sulfate phases suggesting that the reaction shown in Scheme X must have occurred during setting.

$$3\ CuSO_{4(aq)} + 2\ Al_{(s)} \leftrightarrow Al_2(SO_4)_{3(aq)} + 3\ Cu_{(s)}$$

Scheme X. Reaction between copper sulfate and aluminum

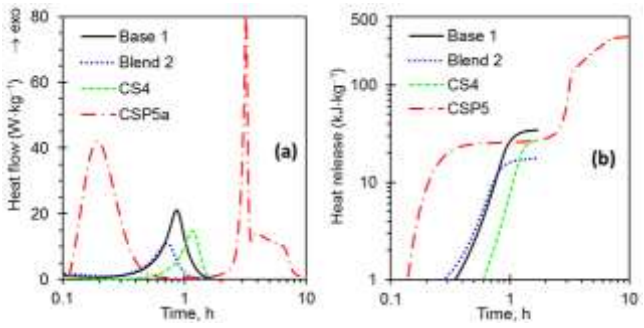

Figure 4. Representative isothermal heat calorimetry results for the Base1, Blend2, S4 and CSP5 compositions: (a) Heat flux, and (b) cumulative heat released. The heat flows were normalized with respect to the total mass of solid powder (4.00 g) plus water (2.00 g).

The heats of hydration for neat α-hemihydrate and β-hemihydrate are reportedly 112 and 100 $kJ \cdot kg^{-1}$ respectively.[11] The measured values listed in Table 4 were lower. The heat of hydration, for the Base1 composition, which comprised a combination of $CaSO_4 \cdot 0.5H_2O$ and Al, was measured as 83 ± 4 $kJ \cdot kg^{-1}$. The values for the Blend2 and S4 were similar. The initial heat released by the CSP5 composition was also of similar magnitude. However, the total heat release including the heat liberated by the reaction of the copper sulfate with the aluminum reached 933 ± 8 $kJ \cdot kg^{-1}$ (based on the mass of the gypsum present in the formulation).

Scanning electron (SEM) images of the fracture surfaces of the cast thermites are presented in Figure 6. The globular aluminum particles are seen interspersed between needle-shaped calcium sulfate crystals formed during the setting reaction. The striking feature revealed by these images is the high porosity of the casts. Measured porosity values are listed in Table 4.

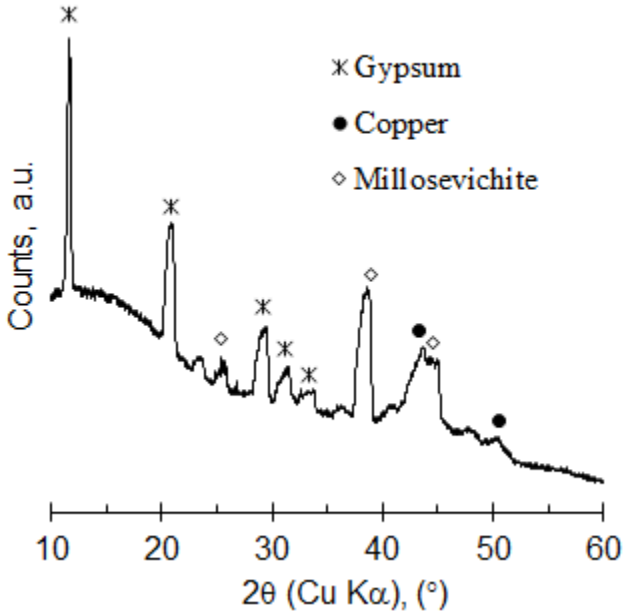

Figure 5. Representative isothermal heat calorimetry results for the Base1, Blend2, S4 and CSP5 compositions

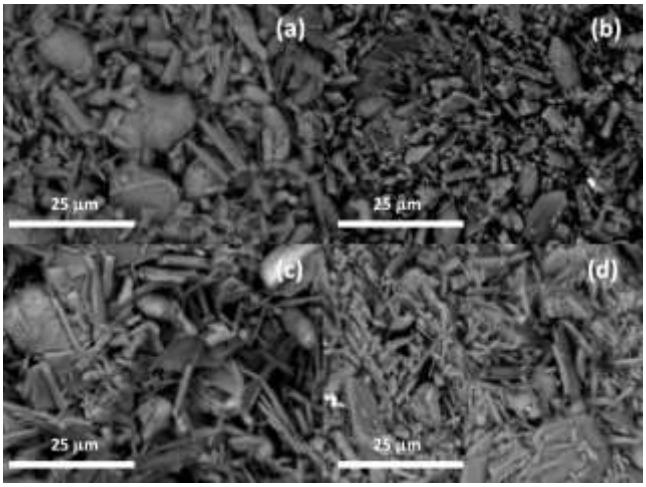

Figure 6. SEM images of fracture surfaces of casts: (a) Base1; (b) Blend 2; (c) S4, and (d) CSP5

Table 5. Compressive strengths (CS) and burn rates (*u*) of castings

	Base1	Blend2	S4	CSP5
CS (MPa)	**2.9±0.2**	**2.3±0.3**	**3.4±0.3**	**4.6±0.2**
***u* (mm·s⁻¹)**				
Unconfined	**12±2**	**18±6**	**13±1**	**10±0.1**
Confined	**819**	**781**	**1016**	**11**

Mechanical properties. The compressive strengths[12] of the casts are reported in Table 5. The compressive strength of composition Base1 was 2.85 ± 0.20 MPa. Partial substitution with the copper sulfate improved the compressive strength to 4.61 ± 0.24 MPa. Casts made with this thermite were also less prone to break when they were removed from the molds. The inclusion of the anhydrous calcium sulfate in Blend2 produced the cast with the lowest compressive strength. This was expected since Blend2 contains less $CaSO_4 \cdot 2H_2O$ than other compositions and the cast strength derives from the interlocking crystal structure developed by the formation of $CaSO_4 \cdot 2H_2O$.

Differential thermal analysis. DTA traces obtained for the individual raw material components and the Base1 composition are presented in Figure 7. The onset temperatures reported in Figure 7 were determined with the Shimadzu TA60 software. The dehydration onset temperatures for the calcium sulfate hemihydrate and for the Base1 composition were 122 °C and 133 °C respectively. The aluminum fuel showed a melting event commencing at 666 °C. The decomposition of $CaSO_4$ commenced at temperatures above 1070 °C. The thermal runaway in Figure 7(a) corresponds to the combustion of the Base1 composition. The ignition onset temperature was 985 °C. The DTA signal for this event looped back on itself. This means that the thermite reaction rapidly heated the whole chamber to a temperature that exceeded the programmed oven temperature. This forced the instrument to cool the oven in order to return to the programmed ramp temperature. While the onset temperature indicates an ignition temperature of about 985 °C, there is also a small exotherm hump with an onset temperature of 907 °C. Its origin is not currently understood.

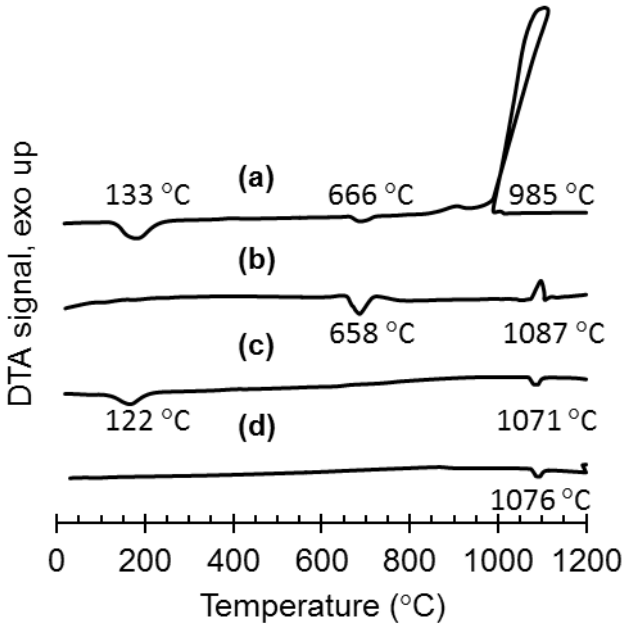

Figure 7. Differential thermal analysis of (a) Base1 thermite with 60 wt-% $CaSO_4 \cdot 2H_2O$ and 40 wt-% Al, (b) raw Al, (c) raw $CaSO_4 \cdot 0.5H_2O$ and (d) raw $CaSO_4$

Open air burn tests. Figure 8(a) shows temperature profiles obtained for the Base1 casts measured during open air burn tests with a pyrometer. They provide an indication of the variability of the burn events. A sharp rise in the reaction temperature is evident at the beginning of the recording and a rapid temperature decrease is observed at the end of the burn. Similarly, the temperature profiles of the various compositions measured during open air burns is shown in Figure 8(b). The more gradual decrease in the temperature observed for composition CSP5 at the end of its burn is attributed to the hot slag that formed which only slowly lost its heat. In contrast, compositions Base1 and Blend2 showed a rapid drop in temperature because the granular residues lost heat more rapidly.

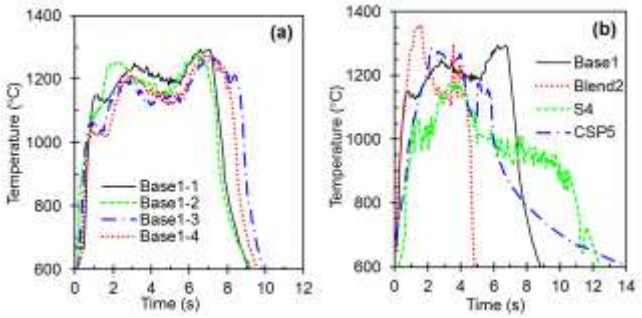

Figure 8. (a) Temperature profile of Base1 thermite recorded with a pyrometer indicating repeatability of burns; (b) Temperature profiles obtained for Base1, Blend2, S4 and CSP5 thermite systems recorded with a pyrometer

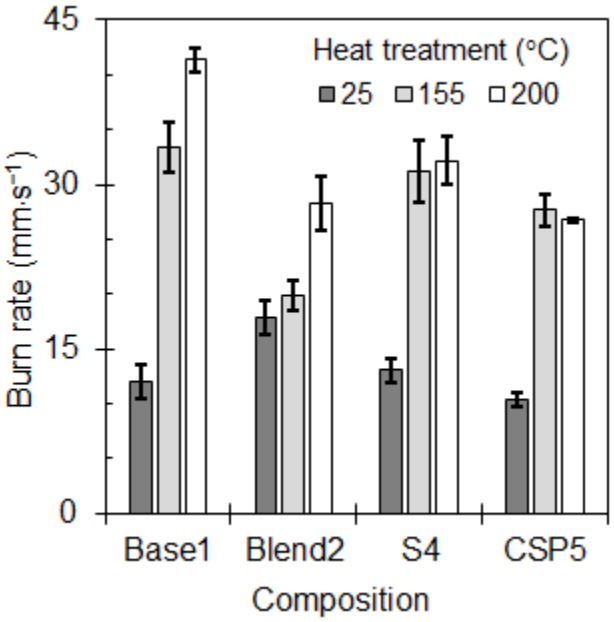

Figure 9. Linear burn rate of untreated casts and after heat-treatment at 155 °C or at 200 °C

The burn rate of casts before and after heat treatments are shown in Figure 9. The base case Base1 produced a burn rate of 12 ± 2 $mm \cdot s^{-1}$. White and yellow powder residues with molten metal spheres were observed in the burn residues. Composition Blend2 produced the fastest burn rate of 18 ± 2 $mm \cdot s^{-1}$. This was expected since the composition contained less calcium sulfate dihydrate ($CaSO_4 \cdot 2H_2O$). Less energy was spent driving

off the waters of hydration implying higher reaction temperatures and thus a faster reaction. Fewer spheres were observed in the residues from Blend2 than from Base1. The slowest burning rate of 10 ± 1 mm·s^{-1} was found for composition CSP5. This could be due to the heat sapping by the inert copper and the less reactive aluminum sulfate present which formed during the setting of the casts. However, a dark blue-green powder residue remained and this suggests that at least part of the copper ions present were not reduced to copper metal. Interestingly, the burning of the CSP5 samples caused fracture of the alumina tiles and they were actually displaced outwards during the burning event.

Figure 9 also shows the effect of heat treatments on the burn rate of the casts. The linear burn rate of Base1 increased from 12 ± 2 mm·s^{-1} (untreated) to 33 ± 2 mm·s^{-1} and 41 ± 1 mm·s^{-1} when treated when heat treated to 155 °C and 200 °C respectively. The more complete dehydration of the Base1 composition produced the fastest burn rate of all the present samples. The objective of the thermal treatments were to release the waters of hydration in $CaSO_4 \cdot 2H_2O$. Since Blend2 contained less $CaSO_4 \cdot 2H_2O$ than the other compositions, it was expected that its burn rate would be the least affected. Blend2 casts showed the least mass change after oven treatment when compared with the other compositions which contained $CaSO_4 \cdot 2H_2O$. On heating this was converted to less hydrated forms resulting in their burn rates being significantly affected. It was observed that heat-treated casts burned significantly faster and that metal-like coatings were deposited on the surface of the alumina tiles that were placed on top to form the roof of the test cages. The oven-treated casts also ignited more easily than casts that were not heat treated.

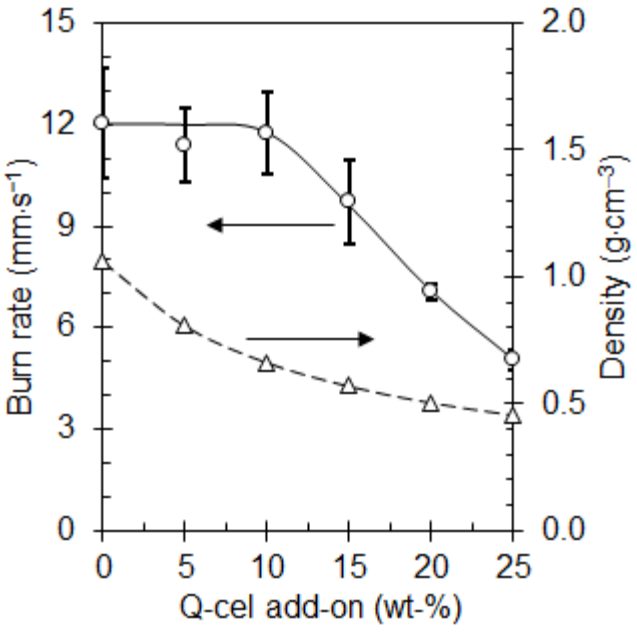

Figure 10. Effect of hollow glass microsphere addition on the cast density and the linear burn rate

Effect of hollow glass microspheres on the burn rate. Figure 10 shows the effect on the burn rate of lowering the cast density by adding hollow glass microspheres to composition Base1. At low loadings, corresponding to higher densities, there was little effect on the burn rate. The burn rate plateau trend held up to 10 wt-% add-on of the glass spheres, i.e. cast densities ranging from 1.06 down to 0.66 g cm^{-3}. Thereafter, a rapid drop in burn rate is observed on inclusion of additional glass spheres. This reduction in the burn rate is ascribed to the glass spheres representing an inert, non-reactive component of the composition in addition to the physical barrier effect they pose to both heat transfer and diffusion of the reactants.

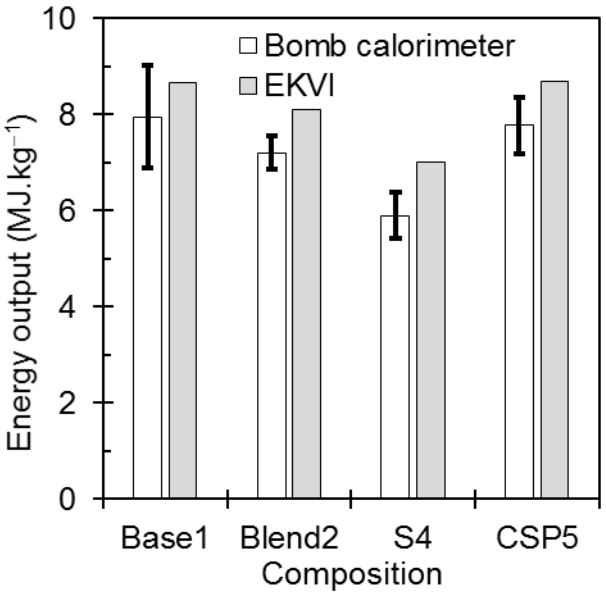

Figure 11. Bomb calorimeter results obtained in helium pressurized to 3 MPa compared to predictions obtained from EKVI simulations

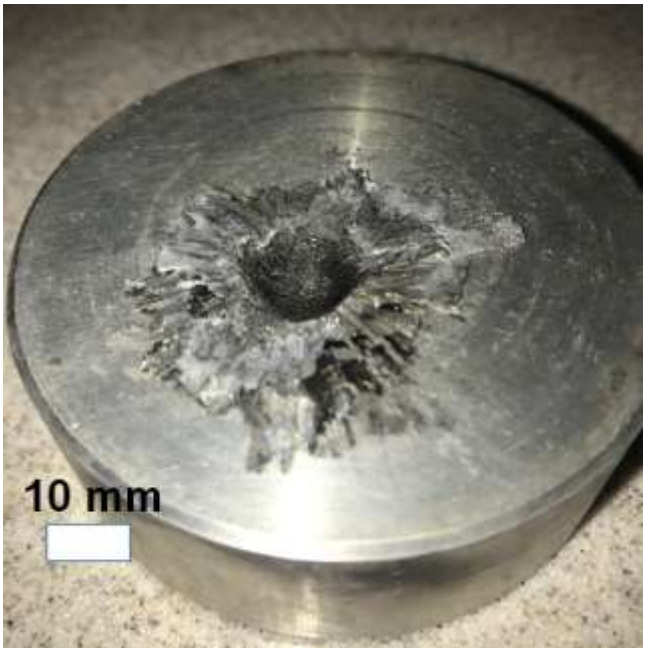

Figure 12. Aluminum blocks showing the hole eroded in a confined burn test by a sample of Blend2 oven-treated at 155 °C

Bomb calorimetry. Bomb calorimeter results obtained in a helium atmosphere are presented in Figure 11. The largest heat releases were 8.0 ± 1.1 $MJ \cdot kg^{-1}$ and 7.8 ± 0.6 $MJ \cdot kg^{-1}$ for the Base1 and CSP5 compositions. Blend2 showed a heat release of 7.2 ± 0.34 $MJ \cdot kg^{-1}$. Composition S4 produced the lowest heat release of 5.9 ± 0.48 $MJ \cdot kg^{-1}$. The experimental bomb calorimeter energy outputs were lower than the theoretical values predicted by the Ekvi simulations by about 8 %. This could indicate that in the actual tests combustion was incomplete.

Confined burn tests. The purpose of the confined burn tests was to establish the ability of the calcium sulfate based thermites to remove aluminum metal. Only samples that were partially dehydrated, by heat-treatment at 155 °C, were tested in these initial tests. The compositions burned significantly faster in the confined state than was recorded in the open air burn tests as shown in Table 5. Interestingly Blend2, and not the fastest burning composition S4, resulted in the largest hole in the aluminum block. Figure 12 shows the diameter and depth of a nearly hemispherical hole created by a Blend2 sample. The average diameter and maximum depth of the hole were 13.6 mm and 7 mm respectively.

CONCLUSIONS

Thermodynamic simulations indicated that a thermite composition, comprising 60 wt-% calcium sulfate dihydrate ($CaSO_4 \cdot 2H_2O$) as oxidant with 40 wt-% aluminum as fuel, has an adiabatic reaction temperature of 2808 °C. Mechanically strong moldings were obtained by casting water-based slurries with a solids content of 65 wt-%. Isothermal heat flow calorimetry showed that the setting reaction was thermally complete within 75 min. The compressive strength, after ambient drying, was 2.85 ± 0.20 MPa. Differential thermal analysis scans at 50 $°C \cdot min^{-1}$ indicated an ignition temperature of 985 °C. The unconfined open burn rate was 12 ± 2 $mm \cdot s^{-1}$ but it was 819 $mm \cdot s^{-1}$ when confined in a phenolic tube. Bomb calorimetry studies in helium at a pressure of 0.1 MPa showed that the energy output of the thermite was 8.0 ± 1.1 $MJ \cdot kg^{-1}$. Partial substitution of the oxidant by copper sulfate pentahydrate led to faster setting, better mechanical properties but a slower burn rate.

ACKNOWLEDGEMENTS

This work is based on the research supported in part by the Council for Scientific and Industrial Research (CSIR) and the Institute of Applied Materials at the University of Pretoria. The opinions, findings and conclusions are those of the authors, and the CSIR accepts no liability whatsoever in this regard.

The authors express their gratitude to Ms. Grizelda du Toit and Afrisam CPE for assistance with isothermal heat flow calorimeter measurements.

REFERENCES

(1) Conkling, J. A. Pyrotechnics. Kirk-Othmer Encyclopedia of Chemical Technology, John Wiley & Sons; **2000**, DOI: 10.1002/0471238961.1625181503151411.a01

(2) Berger, B. Parameters Influencing the Pyrotechnic Reaction. *Propellants Explos. Pyrotech.* **2005**, *30*, 27–35.

(3) Steinhauser, G.; Klapötke, T. M. "Green" pyrotechnics: a chemists' challenge. *Angew. Chem. Int. Ed.* **2008**, *47*, 3330–3347.

(4) Khasainov, B; Comet, M; Veyssiere, B and Spitzer, D. Comparison of Performance of Fast-Reacting Nanothermites and Primary Explosives. *Propellants Explos. Pyrotech*. **2017**, *42(7)*, 754–772.

(5) Comet, M.; Vidick, G.; Schnell, F.; Suma, Y.; Baps, B.; Spitzer, D. Sulfates-based Nanothermites: An Expanding Horizon for Metastable Interstitial Composites. *Angew. Chem. Int. Ed.* **2015**, 4458–4462.

(6) Fitzpatrick, J. A. Hydrogen Gas Generating Propellent Compositions, US Pat US39448153A, **1959**.

(7) Schroder, K. A.; Dass, R. I. Method for Manufacturing Energetic Material Composites, US Pat 9,617,193 B2, **2017**.

(8) Weiser, H. B.; Moreland, F. B. The Setting of Plaster of Paris. *J. Phys. Chem.* **1931**, *36*, 1–30.

(9) Noläng, B. EkviCalc, 4.30; Balinge, Sweden, 1996.

(10) Pöllmann, H.; Kuzel, H.-J.; Meyer, H. W. In Heat-flow Calorimetry in Cement Chemistry. Construction and Application of a Low Cost High Sensitive Calorimeter, 13th International Conference on Cement Microscopy, Tampa, Florida, USA, **1991**, 254–274.

(11) Tydlitát, V.; Tesárek, P.; Cerny, R. Effects of the type of calorimeter and the use of plasticizers and hydrophobizers on the measured hydration heat development of FGD gypsum. *J. Therm. Anal. Calorim*. **2008**, *91*, 791–796.

(12) ASTM Standard Test Method for Compressive Strength of Cylindrical Concrete Specimens. ASTM International: United States, **2017**; Vol. C39/C39M - 17b, 1–8.

Graphical abstract